Progress Report:
Neural Networks for Computed Tomography Imaging Spectroscopy of the Solar Atmosphere

Roy Smart

`roy.smart@montana.edu`

Montana State University, Department of Physics
Bozeman, MT 59717, USA

March 14, 2018

1 Introduction

The goal outlined in my NESSF17 proposal was to classify explosive events (EEs) (Brueckner and Bartoe, 1983) in the solar transition region (TR) according to their 2D spatial structure. I proposed to accomplish this goal using two sounding rocket-borne instruments optimized towards observing EEs, the *Multi-order Solar EUV Spectrograph* (MOSES)(Kankelborg and Thomas, 2001), and the *EUV Snapshot Imaging Spectrograph* (ESIS). MOSES flew successfully in 2006 (Fox et al., 2010) and 2015 Smart et al. (2016), and both instruments are planned to fly in 2019. These instruments are members of a class of spectrographs known as snapshot imaging spectrographs, which can spectrally-resolve a 2D field-of-view (FOV) in a single snapshot, as opposed to imaging spectrographs, such as *Interface Region Imaging Spectrograph* (IRIS) (De Pontieu et al., 2014), which can only spectrally-resolve a 2D FOV through rastering. Snapshot imaging spectrographs are needed to adequately characterize the spatial structure of EEs, since EEs evolve faster than the rastering timescale of IRIS(Kankelborg and Thomas, 2001; De Pontieu et al., 2014).

MOSES and ESIS are a type of snapshot imaging spectograph known as a computed tomography imaging spectrograph (CTIS)(Okamoto and Yamaguchi, 1991), which takes a snapshot of a 2D FOV by simply removing the slit used by imaging spectrographs. Without the slit, space and spectrum become confused, so images are taken at several diffraction orders/angles to provide adequate information about the scene. These images can be interpreted as a spectrally-resolved 2D scene using computed tomography (CT) inversion algorithms, hence the name CTIS. Spectrally-resolving MOSES and ESIS data is an ill-posed inversion problem because they only image in a limited number (3-6) of diffraction orders/angles (Kankelborg and Thomas, 2001).

A brute-force approach to addressing this ill-posed inversion problem would be to use a forward model of a MOSES/ESIS and an a priori model of solar TR spectra to create a dictionary of spectral structures and their corresponding signature on the CTIS detectors. This would allow CTIS observations to be matched to entries in this dictionary to recover a spectrally-resolved scene. I developed an approximation to the above brute-force approach using neural networks (NNs), known as a CTIS inversion neural network (CINN). This approximation aims to spectrally-resolve MOSES and ESIS observations using thousands of IRIS Si IV 1403 Å spectra as a model of the solar TR.

NNs are an efficient regression technique for fitting a curve to an arbitrary set of data (Russel and Norvig, 2010), known as the training data. Our CINNs are a NN designed to invert a function that maps spectral line parameters to their corresponding signal on the CTIS detectors. To accomplish this, we apply a CTIS forward model to a large set of IRIS Si IV 1403 Å spectra and then use the a NN to fit the inverse function. The CTIS forward model is spatially invariant, so it is not necessary to make a neural network large enough to invert an entire CTIS image. Instead, we can implement a neural network that can invert a single pixel, and then convolve this NN with a CTIS observation to construct a spectrally-resolved image. This type of

neural network is known as a convolutional neural network (CNN) and is an important optimization that makes this problem tractable on a modern consumer graphics processing unit (GPU).

We have completed a simple realization of a CINN for the MOSES-06 instrument, the Doppler inversion network (DIN), which reconstructs the Doppler-shift of the He II 304 Å spectral line observed by MOSES-06. We found that our implementation of a DIN was more accurate at reconstructing large Doppler velocities than existing CT algorithms. However, we also discovered that cosmic ray spikes (CRS) in the IRIS Si IV 1403 Å observations were confounding the predictive power of our DIN, motivating the addition of a IRIS despiking routine into our procedure. Existing IRIS despiking routines were ill-suited to processing thousands of IRIS observations, because of the need to manually tune these routines for each unique IRIS observation. Therefore, we developed our own GPU-accelerated despiking routine designed to provide acceptable automated despiking performance across our IRIS dataset.

For the remainder of my NESSF17 proposal (up to 09-01-18), I plan to introduce numerous improvements to our IRIS data pipeline, including the improved despiking routine, and produce a publication describing the application of our DIN to the MOSES-06 dataset. In my proposed schedule for NESSF18, I will develop and produce a publication on an improved CINN with the capability to reconstruct the full spectral line profile of the MOSES-06 observation (dubbed a spectral profile inversion network (SPIN)), and begin development of a EE classification scheme.

A more complete understanding of the mechanisms responsible for explosive events is directly applicable to the NASA Heliophysics Division's objective of "Exploring the physical processes in the space environment from the Sun to the Earth and throughout the solar system" because the dynamics of explosive events are applicable to other regions of the solar atmosphere and may provide insight into long-standing questions about energy transport within the Sun.

2 NESSF17 Progress Report

We presented preliminary results of a SPIN for inverting the MOSES-06 dataset in Section 2.3 of our NESSF17 proposal. An important issue with these results is that they are blurry with respect to the original image. It was expected that we could resolve this issue by creating a larger neural network, but it persisted regardless of the network size. After more research it was determined that this behavior was due our use of the Euclidean norm as a loss function, the function that measures the fit of the NN to the data. This is a well-documented limitation of using the Euclidean norm for image reconstruction (Pathak et al., 2016). It was determined that we would require a more sophisticated loss function, which we will discuss further in Section 4.1, but we decided to first try and solve a simpler problem using our existing architecture.

2.1 Doppler Inversion Network

EEs are characterized by non-thermal Doppler broadening on the order of $100 \, \mathrm{km/s}$, and/or comparable Doppler shifts of an TR emission line (Dere et al., 1989). Therefore, to identify and classify EEs we do not necessarily need to recover the spectral line profile from a CTIS instrument, just the Doppler shift and width of the line profile. Solving for these two parameters is simpler than the spectral line profile since they contain less information. We modified our SPIN that mapped MOSES observations to spectral line profiles, to a DIN that mapped MOSES observations to the *mean* of a spectral line profile, a measurement of Doppler shift. The DIN allows for the extraction of useful plasma parameters while retaining the simplicity of our original method.

Our DIN implementation is a CNN with a 21x1 pixel kernel that is convolved with MOSES observations to calculate the Doppler shift at each pixel. Our training dataset consisted of 4.5k IRIS spectra selected for their high signal-to-noise ratio (SNR) and we also constructed a validation dataset containing the same number of images to test our method against a statistical independent sample. This kernel size represents a window of $\pm 300 \, \mathrm{km/s}$ in MOSES pixels, providing a healthy margin around the typical $100 \, \mathrm{km/s}$ size of EEs(Dere, 1994). For this kernel size, we developed two networks: a *Test* network with 1k free parameters, and a *Final* network with 800k free parameters. In Table 1 we have listed some important properties of these two networks, along with some qualitative measures of their performance. This was done as a preliminary test of the quality of the reconstructed results, as a function of network complexity. We can see that both networks were able to achieve an RMS velocity error better than the theoretical resolution of

	Test	Final
Free Parameters	1.2k	836k
Training Images	4.5k	4.5k
Training time (min)	3	15
RMS error (km/s)	12.7	10.3
Pearson's r	0.500	0.701

Table 1: Description of the characteristics and results of two neural networks tested for this progress report. More comprehensive results from the Final network are presented in later figures.
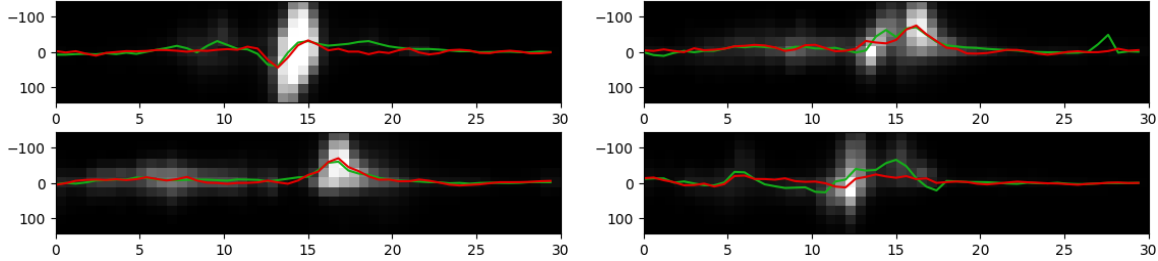

Figure 1: Examples of Doppler inversions. Each image is an IRIS Si IV 1403 Å spectrum rebinned into MOSES resolution. The vertical axis is wavelength (km/s) and the horizontal axis is space (arcsec). The true line center is plotted in green, and the reconstructed line center is plotted in red.

MOSES (29 km/s). Also we will point out that the training time was very short, only 15 minutes for the Final network. This performance is possible thanks to GPU implementations of our NN libraries.

In Figure 1 we have provided a few validation examples of our method, where we have plotted the reconstructed Doppler velocity along with the true velocity for comparison. We chose to show these validation examples since they demonstrated reasonably-high Doppler velocities, characteristic of some types of EEs. We can see that in areas of high signal the network does reasonably well at reproducing the true Doppler shift, while in areas of low signal the Doppler shift is underestimated. We anticipate that the despiking procedure outlined in Section 2.2 will improve results in these low-signal areas, since spikes are more effective at changing the estimated Doppler shift in these areas.

Currently, the smooth multiplicative algebraic reconstruction technique (SMART)(Fox et al., 2010) serves as the de facto standard algorithm for MOSES spectral line profile inversions. In Figure 2a we can see an important test of this algorithm, the Doppler velocity (mean) of the reconstructed spectral line profile, compared to the mean of the original (or true) line profile. This test can be represented as a scatterplot since it consisted of applying SMART to a single SUMER raster.

In Figure 2b we present an analogue of Figure 2a for the DIN calculated using our validation dataset. Since the validation dataset is so large, it would be poorly represented as a scatterplot, so we present it as a column-normalized 2D histogram, where each bin of the histogram has been divided by the sum of its column. This presentation demonstrates the probability of accurately reconstructing the Doppler velocity as a function of the true Doppler velocity. We have also plotted the line of perfect reconstruction, if the algorithm were perfect, all the probability would be in pixels under this line. We calculated Pearson's r of this histogram for both our Test and Final networks, and were able to verify that the addition of more free parameters corresponded to significant improvement in the performance of the network under this metric.

SMART has a systematic tendency to underestimate the reconstructed velocity, a well studied property of this algorithm (Fox, 2011; Rust, 2017). We can see that the DIN does a much better job, on average, of correctly estimating the velocity, however there is still significant underestimation of velocity. We think that this underestimation is at least partially due to CRSs in both the training and validation datasets, which we will discuss in Section 2.2. For now, we consider these results exciting verification of our method, since the DIN method allows for more accurate reconstructions of high-velocity events such as EEs.
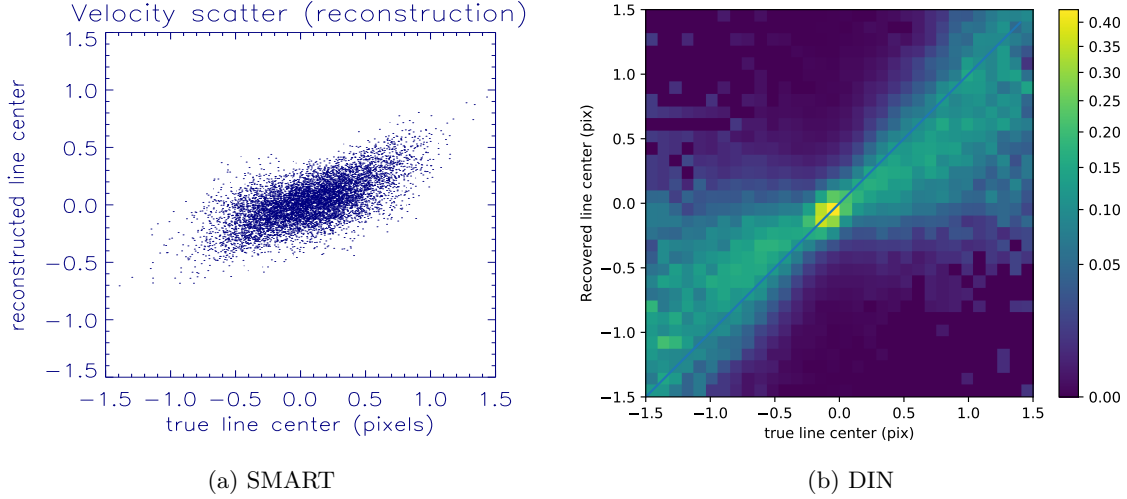
Figure 2: Reconstructed vs. true Doppler velocity using both the standard SMART algorithm (applied to SUMER O III 703.87 Å raster)(Kankelborg and Fox, 2004), and the CINN algorithm (applied to our IRIS Si IV 1403 Å validation dataset). Figure 2a is a scatterplot of the reconstructed velocity vs. true velocity for every pixel in the SUMER raster. Figure 2b is a column-normalized histogram (where each column is an independent, normalized distribution) with the same axes as Figure 2a. Plotted in red is the line of perfect reconstruction.

2.2 Despiking Training Data

Spikes in IRIS observations are a stochastic process, primarily due to ionospheric particles impacting the CCD detectors (Haugan et al., 2013). Removal of spikes in our training dataset is important since the network will become distracted trying to reconstruct the spikes, a futile undertaking. This was not considered to be a serious problem during the proposal phase, as there have been several despiking routines written for IRIS. However we failed to appreciate how difficult it would be to apply these routines in an automated fashion to a large section of the IRIS Si IV 1403 Å dataset.

There are a multitude of despiking routines available on the IDL SolarSoft libraries, such as `nospike.pro`, `array_despike.pro`, `iris_prep_despike.pro`. All these procedures identify spikes using the same method: convolution of some kernel with an image to estimate a local mean and standard deviation, and a hard threshold to exclude pixels some number of standard deviations above the mean. This method is often too aggressive in areas of high signal intensity and not aggressive enough in areas of low signal intensity. In Figure 3, we can see an example of this behavior: the explosive event in the bottom row has become eroded from `iris_prep_despike.pro`, while many of the spikes in the top row are only partially identified. Considering this behavior, to use these procedures we found that we would have to manually tune them for each observation, which would become prohibitive for a training dataset composed of thousands of IRIS observations.

Instead of estimating the mean and standard deviation, our method uses a median-percentile based approach, where pixels are marked as spikes if their value is larger than 99% (for example) of all other pixels with the same median. This is accomplished by calculating a local median for every pixel in the observation, and then constructing a histogram of local median vs. pixel value for each observation. From this histogram, we can then determine the bad pixel threshold as a function of the local median. Finally, this procedure was performed independently along each axis (wavelength, space, time) and we required that a pixel must be above the threshold for all three axes to be marked as a spike. A visualization of this procedure is presented in Figure 4, where we can see the thresholds of each axis overplotted on the histograms used to perform the despiking seen in Figure 3. We have developed a GPU implementation of this despiking procedure, resulting in code that is at least 10x faster than current methods while being much more discriminatory at avoiding false positives and false negatives.

3 Remainder of NESSF17 Schedule

With the exception of exchanging the SPIN development for the DIN development, we are consistent with the schedule given in my NESSF17 proposal, on track for a publication to be submitted before the end date of the proposal period. This publication will cover the motivation, implementation, and validation of our DIN, with applications to the MOSES-06 dataset. We will compare the inversions recovered using the DIN to those calculated using other methods to determine if the DIN is a worthwhile improvement. Our inversions of the MOSES-06 dataset will be available to the public, to support further investigations into this dataset. Also, we will release our despiking routine to the public to promote easier analysis of IRIS data and allow other researchers to adapt the code for their needs.

Before the results of our method can be published, we need to make a few improvements to the training data pipeline such as: the despiking procedure discussed in Section 2.2, a model of the MOSES-06 passband (Fox, 2011), a solar continuum model around He II 304 Å(Fox, 2011), and an accurate noise model for the MOSES-06 detectors Rust (2017). We also need to implement some critical preprocessing steps to the MOSES-06 dataset such as: point-spread function (PSF) deconvolution (Rust, 2017), and spectral contamination removal (Parker and Kankelborg, 2016). Additionally, we need to improve our network architecture to include the width of the spectral line profile. Finally, our validation tests need to be improved, with SMART applied to the same validation set as the DIN, and several simple validation tests such as those in Rust (2017).
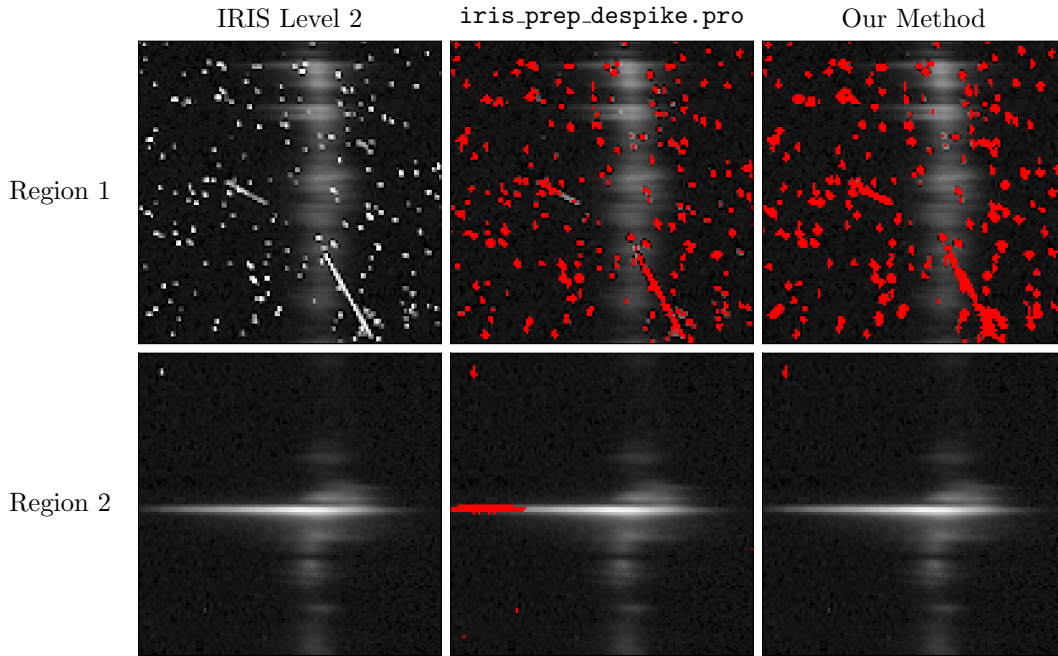
Figure 3: An example of both the standard despiking algorithm and our spike identification algorithm applied to an IRIS Si IV 1403 Å observation gathered at 07:24:26 on 06-16-2015. Pixels containing spikes are marked red by each algorithm. We present cutouts from frames 24 and 50 to demonstrate how susceptible each algorithm is to false spike identifications. The frame on the top row was taken inside the SAA, and provides examples of many types of spikes intended to show the false negatives identified by each algorithm. The frame on the bottom row is an example of an EE, and serves as an example of the false positives identified by each algorithm.

(a) Wavelength   (b) Space   (c) Time

Figure 4: Column-normalized histogram of local median intensity along each axis vs. intensity for the observation in Figure 3. Each column has been divided by its total to understand the distribution of values about a particular median. The 1% and 99% thresholds have been plotted in white.

4   NESSF18 Proposal

We are proposing to continue this research under the NESSF18 solicitation. The results we have obtained so far show that our method is superior to current techniques in term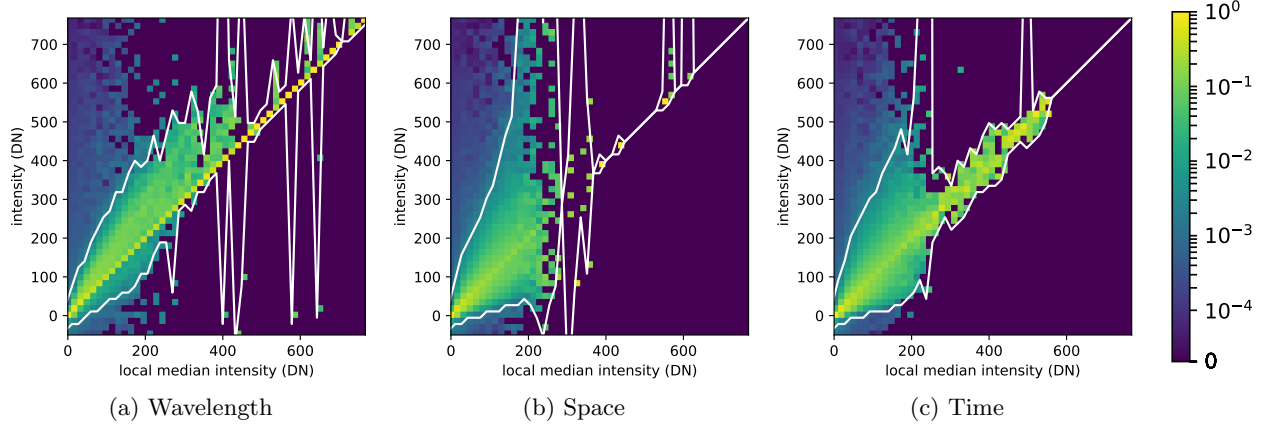s of reconstruction accuracy of Doppler shift. We think this merits additional investigation into using CNN techniques to interpret data from CTIS instruments such as MOSES and ESIS. Furthermore, we have made progress in terms of our CTIS analysis tools, but we haven't yet developed any software to address our ultimate goal of classifying EEs. We plan to implement a more sophisticated SPIN during the first half of the NESSF18 proposal period, and to begin work on an EE classifier during the second half of the proposal period.

4.1   MOSES Inversion GAN

An exciting advancement in using CNNs for image reconstruction has been the development of *adversial loss* as opposed to the Euclidean loss used by our current networks. This concept is expressed in a new type of NN called a generative adversarial network (GAN), developed by Goodfellow et al. (2014). In this type of network, our current DIN is known as the *generator* network, and its output is an input to the *adversary* network. The adversary network's task is to compare the output image of the generator network to the true image and determine which one was created by the generator network. The loss is minimized when the adversary network can't distinguish between the generated image and the true image Isola et al. (2016). This method was recently used for PSF deconvolution of astrophysical images by Schawinski et al. (2017), the results indicate that this is a powerful technique that is well-suited to our inversion problem.

Our plan is to pursue development of a GAN for a MOSES SPIN after the submitting our publication describing the DIN. We expect the development time should be relatively short considering that we can use the training dataset from the DIN. If this MOSES inversion GAN is shows improvement over our current method, we will publish a short article describing the implementation and results of our approach.

4.2   Explosive Event Classification

The literature has conducted extensive analyses of EEs using rastering imaging spectrographs, such as IRIS. They identify EEs as an enhancement of the red and/or blue wings of emission lines forming between 20,000K and 250,000K (Moses et al., 1994). These events are often spectrally classified into two groups: those with enhancements in both wings and those with enhancement in only one wing (Dere et al., 1989). The wings are sometimes displaced from one another by a few thousand kilometers (Dere, 1994), indicating a dynamic spatial structure. Recently, Innes et al. (2015) interpreted EEs as evidence of MHD reconnection through the plasmoid instability, however there have been many other explanations for EEs such as: flows along loops (Teriaca et al., 2004), flows along spicules (Wilhelm, 2000) and plasma ejection and retraction (Huang et al.,

2014). Presently, it is unclear if EEs can be explained by one physical mechanism, or if multiple mechanisms are required to explain their characteristics.

In our NESSF17 proposal we asked: **If these events do arise from multiple mechanisms, can we distinguish different types of explosive events by considering their spatial structure?** To answer this question, the spectrally-resolved images of the solar TR taken using MOSES and later ESIS will be used to isolate EEs and construct a database of events. We will then apply simple *clustering* algorithms, such as k-means (MacQueen, 1967), to test if EEs can naturally be classified into different groups. This is an important first step to see if any obvious classes of EEs can be identified. We intend to present preliminary results of our investigation into this method in our NESSF19 progress report.

ID	Task Name	Duration	Start	Finish
1	NESSF18 Renewal Due Date	0 days	Thu 3/15/18	Thu 3/15/18
2	NESSF19 Renewal Due Date	0 days	Fri 3/15/19	Fri 3/15/19
3	NESSF17 End Date	0 days	Sat 9/1/18	Sat 9/1/18
4	NESSF18 End Date	0 days	Sun 9/1/19	Sun 9/1/19
5	**MOSES Doppler Inversion Network**	**170 days**	**Thu 3/15/18**	**Wed 11/7/18**
6	**Development**	**90 days**	**Thu 3/15/18**	**Wed 7/18/18**
7	Complete Despiking Procedure	1 mon	Thu 3/15/18	Wed 4/11/18
8	IRIS Level 2 Despiking	2 wks	Thu 4/12/18	Wed 4/25/18
9	DIN Development/Testing	1 mon	Thu 4/26/18	Wed 5/23/18
10	MOSES Data Preparation	1 mon	Thu 5/24/18	Wed 6/20/18
11	MOSES Doppler Inversion	2 wks	Thu 6/21/18	Wed 7/4/18
12	Validation Against SMART	2 wks	Thu 7/5/18	Wed 7/18/18
13	**Publication**	**80 days**	**Thu 7/19/18**	**Wed 11/7/18**
14	Writing	2 mons	Thu 7/19/18	Wed 9/12/18
15	Peer Review	1 mon	Thu 9/13/18	Wed 10/10/18
16	Response to Review	1 mon	Thu 10/11/18	Wed 11/7/18
17	**MOSES Inversion GAN**	**140 days**	**Thu 9/13/18**	**Wed 3/27/19**
18	**Development**	**60 days**	**Thu 9/13/18**	**Wed 12/5/18**
19	GAN Research	2 wks	Thu 9/13/18	Wed 9/26/18
20	MIG Development/Validation	2 mons	Thu 9/27/18	Wed 11/21/18
21	MOSES Spectral Inversion	2 wks	Thu 11/22/18	Wed 12/5/18
22	**Publication**	**80 days**	**Thu 12/6/18**	**Wed 3/27/19**
23	Writing	2 mons	Thu 12/6/18	Wed 1/30/19
24	Peer Review	1 mon	Thu 1/31/19	Wed 2/27/19
25	Response to Review	1 mon	Thu 2/28/19	Wed 3/27/19
26	**EE Classifier**	**160 days**	**Thu 1/31/19**	**Wed 9/11/19**
27	**Development**	**80 days**	**Thu 1/31/19**	**Wed 5/22/19**
28	Classifier Research	2 wks	Thu 1/31/19	Wed 2/13/19
29	EEC Development	3 mons	Thu 2/14/19	Wed 5/8/19
30	Compare Results to Literature	2 wks	Thu 5/9/19	Wed 5/22/19
31	**Publication**	**80 days**	**Thu 5/23/19**	**Wed 9/11/19**
32	Writing	2 mons	Thu 5/23/19	Wed 7/17/19
33	Peer Review	1 mon	Thu 7/18/19	Wed 8/14/19
34	Response to Review	1 mon	Thu 8/15/19	Wed 9/11/19
35	**NESSF19 Progress Report**	**20 days**	**Thu 2/14/19**	**Wed 3/13/19**
36	Writing	1 mon	Thu 2/14/19	Wed 3/13/19

References

G. E. Brueckner and J.-D. F. Bartoe. Observations of high-energy jets in the corona above the quiet sun, the heating of the corona, and the acceleration of the solar wind. *The Astrophysical Journal*, 272:329–348, September 1983. doi: 10.1086/161297.

B. De Pontieu, A. M. Title, J. R. Lemen, G. D. Kushner, D. J. Akin, B. Allard, T. Berger, P. Boerner, M. Cheung, C. Chou, J. F. Drake, D. W. Duncan, S. Freeland, G. F. Heyman, C. Hoffman, N. E. Hurlburt, R. W. Lindgren, D. Mathur, R. Rehse, D. Sabolish, R. Seguin, C. J. Schrijver, T. D. Tarbell, J.-P. Wülser, C. J. Wolfson, C. Yanari, J. Mudge, N. Nguyen-Phuc, R. Timmons, R. van Bezooijen, I. Weingrod, R. Brookner, G. Butcher, B. Dougherty, J. Eder, V. Knagenhjelm, S. Larsen, D. Mansir, L. Phan, P. Boyle, P. N. Cheimets, E. E. DeLuca, L. Golub, R. Gates, E. Hertz, S. McKillop, S. Park, T. Perry, W. A. Podgorski, K. Reeves, S. Saar, P. Testa, H. Tian, M. Weber, C. Dunn, S. Eccles, S. A. Jaeggli, C. C. Kankelborg, K. Mashburn, N. Pust, L. Springer, R. Carvalho, L. Kleint, J. Marmie, E. Mazmanian, T. M. D. Pereira, S. Sawyer, J. Strong, S. P. Worden, M. Carlsson, V. H. Hansteen, J. Leenaarts, M. Wiesmann, J. Aloise, K.-C. Chu, R. I. Bush, P. H. Scherrer, P. Brekke, J. Martinez-Sykora, B. W. Lites, S. W. McIntosh, H. Uitenbroek, T. J. Okamoto, M. A. Gummin, G. Auker, P. Jerram, P. Pool, and N. Waltham. The interface region imaging spectrograph (iris). *Solar Physics*, 289(7):2733–2779, 2014. ISSN 1573-093X. doi: 10.1007/s11207-014-0485-y. URL http://dx.doi.org/10.1007/s11207-014-0485-y.

K. P. Dere, J.-D. F. Bartoe, and G. E. Brueckner. Explosive events in the solar transition zone. *Solar Physics*, 123:41–68, March 1989. doi: 10.1007/BF00150011. URL http://adsabs.harvard.edu/abs/1989SoPh..123...41D.

K.P. Dere. Explosive events, magnetic reconnection, and coronal heating. *Advances in Space Research*, 14 (4):13 – 22, 1994. ISSN 0273-1177. doi: http://dx.doi.org/10.1016/0273-1177(94)90154-6. URL //www.sciencedirect.com/science/article/pii/0273117794901546.

J. L. Fox, C. C. Kankelborg, and R. J. Thomas. A Transition Region Explosive Event Observed in He II with the MOSES Sounding Rocket. *ApJ*, 719:1132–1143, Aug 2010. doi: 10.1088/0004-637X/719/2/1132. URL http://adsabs.harvard.edu/abs/2010ApJ...719.1132F.

James Lewis Fox. *Snapshot imaging spectroscopy of the solar transition region the multi-order solar EUV spectrograph (MOSES) sounding rocket mission.* 2011.

Ian J. Goodfellow, Jean Pouget-Abadie, Mehdi Mirza, Bing Xu, David Warde-Farley, Sherjil Ozair, Aaron Courville, and Yoshua Bengio. Generative adversarial networks. June 2014.

Stein V. H. Haugan, John Serafin, and Richard Shinen. Iris technical note 15 pipeline despiking procedure. Technical report, Lockheed Martin, Solar Astrophysics Laboratory, June 2013.

Zhenghua Huang, Maria S. Madjarska, Lidong Xia, J. G. Doyle, Klaus Galsgaard, and Hui Fu. Explosive events on a subarcsecond scale in iris observations: A case study. *The Astrophysical Journal*, 797(2):88, 2014. URL http://stacks.iop.org/0004-637X/797/i=2/a=88.

D. E. Innes, L.-J. Guo, Y.-M. Huang, and A. Bhattacharjee. Iris si iv line profiles: An indication for the plasmoid instability during small-scale magnetic reconnection on the sun. *The Astrophysical Journal*, 813 (2):86, 2015. URL http://stacks.iop.org/0004-637X/813/i=2/a=86.

P. Isola, J.-Y. Zhu, T. Zhou, and A. A. Efros. Image-to-Image Translation with Conditional Adversarial Networks. *ArXiv e-prints*, November 2016.

C. C. Kankelborg and J. L. Fox. Fast Inversion of MOSES Data. In *American Astronomical Society Meeting Abstracts #204*, volume 36 of *Bulletin of the American Astronomical Society*, page 794, May 2004.

Charles C. Kankelborg and Roger J. Thomas. Simultaneous imaging and spectroscopy of the solar atmosphere: advantages and challenges of a 3-order slitless spectrograph. *Proc. SPIE*, 4498:16–26, 2001. doi: 10.1117/12.450074. URL http://dx.doi.org/10.1117/12.450074.

J. MacQueen. Some methods for classification and analysis of multivariate observations. In *Proceedings of the Fifth Berkeley Symposium on Mathematical Statistics and Probability, Volume 1: Statistics*, pages 281–297, Berkeley, Calif., 1967. University of California Press. URL `https://projecteuclid.org/euclid.bsmsp/1200512992`.

D. Moses, J. W. Cook, J.-D. F. Bartoe, G. E. Brueckner, K. P. Dere, D. F. Webb, J. M. Davis, J. W. Harvey, F. Recely, S. F. Martin, and H. Zirin. Solar fine scale structures in the corona, transition region, and lower atmosphere. *ApJ*, 430:913–924, August 1994. doi: 10.1086/174461.

Takayuki Okamoto and Ichirou Yamaguchi. Simultaneous acquisition of spectral image information. *Opt. Lett.*, 16(16):1277–1279, Aug 1991. doi: 10.1364/OL.16.001277. URL `http://ol.osa.org/abstract.cfm?URI=ol-16-16-1277`.

J. Parker and C. Kankelborg. Determining the Spectral Content of MOSES Images. In *AAS/Solar Physics Division Abstracts #47*, volume 47 of *AAS/Solar Physics Division Meeting*, page 2.04, May 2016.

D. Pathak, P. Krahenbuhl, J. Donahue, T. Darrell, and A. A. Efros. Context Encoders: Feature Learning by Inpainting. *ArXiv e-prints*, April 2016.

Stuart Russel and Peter Norvig. *Artificial Intelligence: A Modern Approach*. Pearson Education, Upper Saddle River, New Jersey 07458, 3rd edition, 2010.

Thomas Rust. Explosive events in the quiet sun: Extreme ultraviolet imaging spectroscopy instrumentation and observations, January 2017. URL `http://search.proquest.com/docview/1952045621/`.

K. Schawinski, C. Zhang, H. Zhang, L. Fowler, and G. K. Santhanam. Generative adversarial networks recover features in astrophysical images of galaxies beyond the deconvolution limit. *Monthly Notices of the Royal Astronomical SocietyS*, 467:L110–L114, May 2017. doi: 10.1093/mnrasl/slx008.

R. Smart, H. Courrier, and C. Kankelborg. Preliminary Results of the MOSES II 2015 Flight. In *AAS/Solar Physics Division Meeting*, volume 47 of *AAS/Solar Physics Division Meeting*, page 309.01, May 2016. URL `http://adsabs.harvard.edu/abs/2016SPD....4730901S`.

L. Teriaca, D. Banerjee, A. Falchi, J. G. Doyle, and M. S. Madjarska. Transition region small-scale dynamics as seen by SUMER on SOHO. *Astronomy & Astrophysics*, 427:1065–1074, December 2004. doi: 10.1051/0004-6361:20040503.

K. Wilhelm. Solar spicules and macrospicules observed by SUMER. *Astronomy & Astrophysics*, 360:351–362, August 2000.

5   List of Acronyms

TR transition region

EE explosive event

CT computed tomography

CTIS computed tomography imaging spectrograph

MOSES *Multi-order Solar EUV Spectrograph*

ESIS *EUV Snapshot Imaging Spectrograph*

EUV extreme ultraviolet

FOV field-of-view

NN neural network

CNN convolutional neural network

SMART smooth multiplicative algebraic reconstruction technique

SAA South-Atlantic Anamoly

CINN CTIS inversion neural network

DIN Doppler inversion network

SPIN spectral profile inversion network

IRIS *Interface Region Imaging Spectrograph*

CRS cosmic ray spikes

GPU graphics processing unit

GAN generative adversarial network

SNR signal-to-noise ratio

PSF point-spread function